Computational Energy Science

Vol. 3, No. 1, p. 5-13, 2026

Original article

Selective displacement versus physical displacement: Transport-mechanism discrimination of hydrogen and helium under CO_2 flooding in natural hydrogen-helium reservoirs

Runjing Guan[1]*, Shuai Pang[2]

[1]*College of New Energy, China University of Petroleum (East China), Qingdao 266580, P. R. China*
[2]*China Petroleum Engineering & Construction Corporation (CPECC), Beijing 100120, P. R. China*

Keywords:
Natural hydrogen
helium
CO_2 flooding
transport mechanism
selective displacement
heterogeneity
dimensionless criterion

Cited as:
Guan, R., Pang, S. Selective displacement versus physical displacement: Transport-mechanism discrimination of hydrogen and helium under CO_2 flooding in natural hydrogen-helium reservoirs. Computational Energy Science, 2026, 3(1): 5-13.
https://doi.org/10.46690/compes.2026.01.02

Abstract:
Natural hydrogen and helium commonly co-accumulate in the subsurface, yet their transport mechanisms differ in a way that has not been captured quantitatively. Hydrogen adsorbs weakly and dissolves slightly, so its transport couples adsorption, advection, and diffusion; helium is inert, so its transport is dominated by advection with Knudsen-enhanced diffusion. We examine how this divergence unfolds during CO_2 flooding, which recovers the two gases while also sequestering carbon. A two-dimensional multicomponent model that couples competitive Langmuir adsorption, Henry dissolution, component-dependent diffusion, and a heterogeneous log-normal permeability field is used. Two results stand out. First, a dimensionless Damköhler–Péclet criterion separates the three gases into distinct transport regimes, with retardation factors of 1.001 (He), 1.287 (H_2), and 1.958 (CO_2), and the retention-time difference between H_2 and He grows monotonically with the adsorption Damköhler number before saturating. Second, a displacement-efficiency coefficient derived from competitive adsorption shows that CO_2 liberates essentially all adsorbed hydrogen (efficiency $\rightarrow$ 1) but leaves helium unaffected (efficiency $\equiv$ 0); CO_2 flooding thus operates on hydrogen by selective displacement and on helium by physical displacement. The unretarded helium accumulates as an enriched slug ahead of the retarded hydrogen and the CO_2 front, reaching a mole-fraction peak of 0.407 from an initial 0.15 even in a strongly heterogeneous reservoir, which provides a basis for in situ separation of the two gases.

1. Introduction

The transition toward low-carbon energy systems has stimulated rapidly growing interest in natural, or geologic, hydrogen as a potentially low-emission subsurface energy resource (Zgonnik, 2020; Ballentine et al., 2025; Mao et al., 2025). Natural hydrogen can be generated through several geological processes, among which water–rock reactions involving Fe-bearing minerals, including serpentinization of ultramafic rocks, constitute an important abiotic pathway (Zgonnik, 2020; Ballentine et al., 2025; Mao et al., 2025). Where economically recoverable accumulations occur, natural hydrogen may provide a low-emission primary energy resource while reducing reliance on the energy-intensive processes used to manufacture hydrogen (Mao et al., 2025). Helium is also an irreplaceable gas for superconducting magnets, semiconductor fabrication, and cryogenics (Li et al., 2024). Crustal helium is generated predominantly by radiogenic decay of U- and Th-bearing minerals and subsequently migrates through sedimentary and structural pathways before accumulation (Li et al., 2024).

Natural hydrogen and helium can co-occur within the same sedimentary basin and, in favorable settings, form joint exploration targets (Wei et al., 2025). Although their dominant source mechanisms differ, with water–rock reactions important for H_2 and radiogenic decay important for crustal He, the two gases can occur within overlapping deep-fluid systems (Li et al., 2024; Ballentine et al., 2025; Wei et al., 2025). Studies

Yandy Scientific Press

*Corresponding author.
E-mail address: *b26150015@s.upc.edu.cn (R. Guan); pangshuaitc@163.com (S. Pang).

3007-5602 © The Author(s) 2024.
Received January 8, 2026; revised February 7, 2026; accepted March 11, 2026; available online March 16, 2026.

of petroliferous basins indicate that deep faults and fractures can provide migration pathways for He and may also connect natural-H_2 occurrences in the same basin (Li et al., 2024; Wei et al., 2025). These examples show that joint accumulation depends on the local relationship among sources, migration pathways, and effective seals, but they do not establish a universal shared pathway (Li et al., 2024; Wei et al., 2025). Joint exploration for natural hydrogen and helium is therefore receiving attention in several sedimentary-basin settings (Mao et al., 2025; Wei et al., 2025). Their co-production, however, remains less understood than conventional gas production because the two resources are commonly treated as a single light-gas component rather than as species with different transport behavior.

The distinction matters. Hydrogen exhibits weak but measurable physisorption on clay minerals and organic-rich reservoir rocks (Wang et al., 2023; Wolff-Boenisch et al., 2023; Alanazi et al., 2024; Zhang et al., 2024). H_2 also partitions into formation water and brine, although its aqueous solubility remains substantially lower than that of CO_2 under comparable conditions (Sander, 2023; Chabab et al., 2024). These properties motivate treating H_2 transport as a coupled adsorption-advection-diffusion process in the present framework. In the present model, helium is treated as non-adsorbing. Its low aqueous solubility is supported by noble-gas solubility data (Potter and Clynne, 1978), while its effective diffusion includes Knudsen and gas-slip contributions as modeling assumptions. The Knudsen contribution is motivated by small-pore membrane transport (Scholes and Ghosh, 2017). During CO_2 injection, CO_2 has a substantially stronger affinity for clay and organic surfaces than H_2, and competitive adsorption therefore suppresses H_2 surface occupancy when the two gases coexist (Alanazi et al., 2023, 2024; Muther and Dahaghi, 2024; Zhang et al., 2024; Zhang et al., 2024; Al-Harbi et al., 2025). Dynamic breakthrough experiments further indicate that CO_2 can modify H_2 displacement and recovery behavior (Li et al., 2025). On this basis, we distinguish two mechanisms in the present study: Selective displacement for H_2 and physical displacement for He. This distinction is physically clear but has not been quantified, and no criterion exists to discriminate the two mechanisms or predict their effect on breakthrough timing and recovery.

Two gaps follow. First, although dimensionless groups have recently been used to characterize pore-scale H_2 and CO_2 transport (Purswani et al., 2024), a coupled adsorption-Damköhler–Péclet framework for discriminating H_2, He, and CO_2 transport in natural H_2–He reservoirs has not, to our knowledge, been established. Second, despite extensive evidence for preferential CO_2 adsorption over H_2 (Alanazi et al., 2023, 2024; Muther and Dahaghi, 2024; Zhang et al., 2024; Zhang et al., 2024; Al-Harbi et al., 2025; Li et al., 2025), a field-scale quantitative metric explicitly distinguishing selective adsorption-driven displacement from purely physical displacement remains lacking to our knowledge.

This paper addresses both gaps. We build a multicomponent transport model for a two-dimensional natural hydrogen–helium reservoir that integrates Langmuir competitive adsorption, Henry dissolution, component-dependent effective diffusion (with Knudsen enhancement of helium), and a heterogeneous log-normal permeability field. On this basis, we make two contributions: (i) A dual dimensionless criterion comprising an adsorption Damköhler number and an advection-diffusion Péclet number, which classifies H_2 as adsorption-advection-diffusion controlled, He as advection-dominant with Knudsen enhancement, and CO_2 as strongly retarded by adsorption; and (ii) a displacement-efficiency coefficient derived from the cross-coupling terms of the extended Langmuir isotherm, which distinguishes selective displacement ($\eta(H_2) \to 1$) from physical displacement ($\eta(\mathrm{He}) \equiv 0$). The first criterion is validated by the monotonic and then saturating increase in the H_2–He retention-time difference with the Damköhler number. Section 2 describes the model and criteria, Section 3 presents the results, and Section 4 concludes.

2. Methodology

2.1 Physical model and assumptions

We consider a two-dimensional, isothermal, single-gas-phase multicomponent system representing a natural hydrogen–helium reservoir subjected to CO_2 injection. The gas phase contains H_2 (component 1), He (component 2), and CO_2 (component 3), transported through a porous medium that also holds immobile connate water. The following assumptions are adopted: (i) The gas phase is the only mobile phase, while connate water is treated as immobile but permits equilibrium gas dissolution represented by a simplified Henry-law partitioning model (Sander, 2023; Chabab et al., 2024); (ii) flow is isothermal and governed by Darcy's law, with the gas treated as ideal; (iii) H_2 and CO_2 adsorb following the extended Langmuir isotherm (Kapoor et al., 1990; Alanazi et al., 2023, 2024; Muther and Dahaghi, 2024; Zhang et al., 2024; Zhang et al., 2024; Al-Harbi et al., 2025), while He is modeled as non-adsorbing; (iv) molecular diffusion is component-dependent, with Knudsen diffusion and slip flow included as effective model contributions for He; the kinetic diameters used to motivate this approximation are about 2.60 Å for He and 2.89 Å for H_2 (Scholes and Ghosh, 2017); and (v) the rock is rigid, with heterogeneity represented by a correlated log-normal permeability field.

2.2 Governing equations

For component k, the mass balance per unit rock volume reads:

$$\frac{\partial}{\partial t}\left[\phi S_g c_k + (1-\phi)\rho_s q_k + \phi S_w H_k R T c_k\right] + \nabla\cdot(u c_k) = \nabla\cdot(\phi S_g D_k \nabla c_k) \tag{1}$$

where ϕ is porosity; S_g and S_w are the gas and water saturations ($S_g + S_w = 1$); ρ_s is the rock density; q_k is the adsorbed amount; H_k is the Henry constant; R is the gas constant; T is the temperature; c_k is the gas-phase molar concentration; D_k is the effective diffusion coefficient; and u is the Darcy velocity. The three storage terms in brackets represent free gas, adsorbed gas, and dissolved gas. The concentration is related to the molar fraction y_k by $c_k = y_k c_{\mathrm{ref}}$, where $c_{\mathrm{ref}} = p/(RT)$.

The Darcy velocity follows from mass conservation and Darcy's law. Under the line-drive configuration used here (constant-pressure injection on the left, constant-pressure production on the right, and no-flow boundaries at the top and bottom), the pressure field for a heterogeneous permeability $k(x,y)$ obeys:

$$\nabla\cdot\left(\frac{k}{\mu}\nabla p\right)=0 \tag{2}$$

with $u=-(k/\mu)\nabla p$, where μ is the gas viscosity. Face transmissibilities are computed by harmonic averaging of adjacent cell permeabilities.

2.3 Constitutive relations

Competitive adsorption is represented with the extended Langmuir isotherm (Kapoor et al., 1990):

$$q_k=\frac{q_{\max,k}b_kc_k}{1+\sum_j b_jc_j} \tag{3}$$

where $q_{\max,k}$ is the maximum adsorption capacity and b_k is the adsorption affinity. The cross-coupling terms $\partial q_k/\partial c_j$ $(j\neq k)$ are strictly negative. Physically, this formulation represents competitive displacement: An increase in the concentration of strongly adsorbing CO_2 suppresses the adsorbed amount of weakly adsorbing H_2, consistent with recent experiments and molecular simulations (Alanazi et al., 2023, 2024; Muther and Dahaghi, 2024; Zhang et al., 2024; Zhang et al., 2024; Al-Harbi et al., 2025; Li et al., 2025). Dissolution in connate water is represented by the simplified Henry-law relation $c_{w,k}=H_kp_k=H_kRTc_k$ (Sander, 2023; Chabab et al., 2024). The effective diffusion coefficient D_k includes bulk molecular diffusion and, for helium, modeled contributions from Knudsen diffusion and slip flow. The latter approximation is motivated by the small kinetic diameter of He and small-pore membrane transport (Scholes and Ghosh, 2017), rather than by a direct rock-scale measurement. Table 1 lists representative transport parameters used for the mechanistic simulations. The Henry constants are guided by compiled and experimental aqueous-solubility data (Potter and Clynne, 1978; Sander, 2023; Chabab et al., 2024), whereas the adsorption contrast follows recent measurements and simulations (Alanazi et al., 2023, 2024; Wang et al., 2023; Wolff-Boenisch et al., 2023; Muther and Dahaghi, 2024; Zhang et al., 2024; Zhang et al., 2024; Al-Harbi et al., 2025). The effective diffusivities and adsorption coefficients are representative values selected to span the target transport regimes rather than a field-specific property set.

Table 1. Representative transport parameters used for the mechanistic simulations.

Parameter	H_2	He	CO_2
D_k (m^2/s)	5.0×10^{-7}	1.5×10^{-6}	2.0×10^{-7}
$q_{\max,k}$ (mol/kg)	0.40	1.0×10^{-4}	0.25
b_k (m^3/mol)	2.0×10^{-4}	1.0×10^{-8}	4.0×10^{-4}
H_k (mol/(m^3·Pa))	7.8×10^{-6}	3.7×10^{-6}	3.3×10^{-4}

2.4 Dimensionless transport-mechanism classification

To discriminate the transport mechanisms, we introduce two dimensionless groups. The adsorption Damköhler number quantifies the ratio of adsorption capacity to convective capacity in the dilute limit:

$$Da_k=\frac{(1-\phi)\rho_s}{\phi S_g}q_{\max,k}b_k \tag{4}$$

and the advection–diffusion Péclet number quantifies the ratio of convection to diffusion:

$$\mathrm{Pe}_k=\frac{uL}{D_k} \tag{5}$$

where u is a characteristic Darcy velocity and L a characteristic length. The effective retardation factor of component k — the ratio of its apparent velocity to that of a non-adsorbing tracer is:

$$R_k=1+\frac{(1-\phi)\rho_s}{\phi S_g}\frac{\partial q_k}{\partial c_k} \tag{6}$$

Which reduces to $R_k\approx1+\mathrm{Da}_k$ in the dilute limit. The three components occupy distinct regimes of the Da–Pe plane: Helium ($\mathrm{Da}\to0$, large Pe) is advection-dominant with Knudsen enhancement; hydrogen (intermediate Da) is of the adsorption-advection-diffusion type; carbon dioxide (large Da, small Pe) is strongly retarded. This classification is the first contribution of the paper.

2.5 Displacement-efficiency coefficient

To quantify the distinction between selective displacement (CO_2 liberating adsorbed H_2) and physical displacement (CO_2 pushing He by bulk flow), we define the displacement-efficiency coefficient:

$$\eta_k=1-\frac{q_k^{\mathrm{final}}}{q_k^{\mathrm{init}}} \tag{7}$$

where $q_{k,\mathrm{initial}}$ and $q_{k,\mathrm{final}}$ are the total adsorbed amounts of component k before and after CO_2 flooding. Under the assumption that He is non-adsorbing, $\eta(\mathrm{He})=0$. In the present simulations, competitive CO_2 adsorption drives $\eta(H_2)$ toward unity. The direction of this modeled response is consistent with published adsorption and breakthrough studies (Alanazi et al., 2023, 2024; Muther and Dahaghi, 2024; Zhang et al., 2024; Zhang et al., 2024; Al-Harbi et al., 2025; Li et al., 2025) but its magnitude is specific to the present parameterization. Because a ratio $\eta(H_2)/\eta(\mathrm{He})$ is undefined when $\eta(\mathrm{He})=0$, we use the ordered pair $(\eta(H_2),\eta(\mathrm{He}))$ as the finite quantitative discriminator: Values approaching $(1,0)$ identify selective displacement of H_2 together with purely physical displacement of He.

2.6 Numerical methods

Eq. (1) is solved by explicit operator splitting. The advection-diffusion step advances the total storage using a second-order MUSCL reconstruction with the Superbee limiter for the streamwise fluxes and first-order upwinding for

the transverse fluxes (Van Leer, 1979; Roe, 1986). Diffusion is discretized by central differences. The adsorption–equilibration step redistributes the total storage between the free-gas and adsorbed phases by solving the nonlinear system $A_{\mathrm{lin},k}y_k + B_{\mathrm{ads}}q_k(y) = M_k$ by Newton iteration, where $A_{\mathrm{lin},k} = (\phi S_g + \phi S_w H_k RT)c_{\mathrm{ref}}$ and $B_{\mathrm{ads}} = (1-\phi)\rho_s$; the 3×3 Jacobian is inverted analytically in vectorized form. The left boundary is held at the injection composition (pure CO_2), and the right boundary is a convective outflow with zero-gradient composition.

2.7 Heterogeneous field generation

A spatially correlated Gaussian field (correlation length $\approx$ 5 grid blocks, fixed random seed) is mapped to a log-normal permeability field with a mean of 50 mD and a $\log_{10}$ standard deviation of 0.5, spanning about 3-1,059 mD in the realization used here. The porosity field is positively correlated with permeability, $\phi = \phi_{\mathrm{mean}} + a\,(\log_{10} k - \langle \log_{10} k \rangle)$, bounded to $\phi \in [0.08, 0.24]$.

2.8 Model validation

The model was checked against: (i) The linear-equilibrium relationship between chromatographic retention time and retention factor (Chabab et al., 2024), expressed in the notation of the present model as $t_{R,k} = t_0\left(1 + \mathrm{Da}_{\mathrm{chord},k}\right)$; (ii) a grid-convergence study (the helium enrichment peak is resolved only for $N_x \geq 200$); and (iii) a global mass-conservation check, with recovery computed from the difference between the initial and remaining storage and capped at 100%. A comparison of first-order upwind and MUSCL confirmed that the second-order limiter preserves the sharp helium-enrichment front, whereas first-order upwind smears it.

3. Results and discussion

3.1 Transport-mechanism classification

Table 2 reports the retardation factors computed from Eq. (6) under the initial conditions, decomposed into adsorption (R_{ads}) and dissolution (R_{diss}) contributions. These factors are intrinsic material properties within the present parameterization and do not depend on whether the permeability field is homogeneous or heterogeneous.

The ordering $R(\mathrm{He}) < R(\mathrm{H_2}) < R(\mathrm{CO_2})$ matches the ordering of the adsorption Damköhler numbers, $\mathrm{Da(He)} \approx 10^{-8} \ll \mathrm{Da}(H_2) = 1.34 < \mathrm{Da}(CO_2) = 1.67$. Helium is essentially unretarded, hydrogen moderately retarded, and carbon dioxide strongly retarded. The Da–Pe framework thus cleanly separates the three components into distinct transport regimes.

3.2 Heterogeneous reservoir field

Fig. 1 shows the heterogeneous log-normal permeability field and the associated porosity field. The permeability spans more than two orders of magnitude, from about 3 to 1,059 mD, organized into elongated high- and low-permeability bands with a correlation length of roughly 5 m. The porosity follows the permeability through a positive correlation, ranging from 0.08 to 0.24. In this realization, the correlated structure creates preferential flow paths through high-permeability bands and low-permeability lenses that the injected CO_2 must circumvent. Recent underground gas-storage studies similarly show that reservoir architecture and permeability heterogeneity affect gas mixing and recovery (Bo et al., 2024; Khandoozi et al., 2025; Lu et al., 2025).

3.3 Saturation evolution and staged recovery

Fig. 2 shows the evolution of the three molar-fraction fields under CO_2 flooding in the heterogeneous reservoir. Three features stand out. First, the displacement front is strongly distorted: It curves around low-permeability lenses and advances fastest along high-permeability channels, leaving bypassed pockets of hydrogen-rich gas in low-permeability regions. Second, helium is preferentially swept ahead of the front and accumulates in an enriched slug that propagates toward the production well ahead of the retarded hydrogen. Third, the CO_2 front arrives early along preferential channels, reaching the producer before the reservoir is swept clean. The modeled sensitivity of mixing and recovery to reservoir architecture is consistent with recent H_2 cushion-gas simulations (Bo et al., 2024; Khandoozi et al., 2025; Lu et al., 2025).

The production history (Fig. 3) preserves the temporally staged character established for the homogeneous case, but with two quantitative changes. The helium mole fraction rises from its initial 0.15 to a peak of 0.407 at about 0.75 PV, and CO_2 breakthrough occurs at about 1.11 PV. Both values are lower than their homogeneous counterparts (peak 0.541, breakthrough 1.60 PV) because heterogeneity disperses the helium slug and opens preferential channels for CO_2. This behavior is consistent with the established effect of reservoir heterogeneity on gas mixing and recovery (Bo et al., 2024; Khandoozi et al., 2025; Lu et al., 2025). Despite this weakening, the helium enrichment remains substantial (2.7-fold), and the sequence remains unchanged: Original mixture, helium-enriched slug, hydrogen-rich tail, and CO_2.

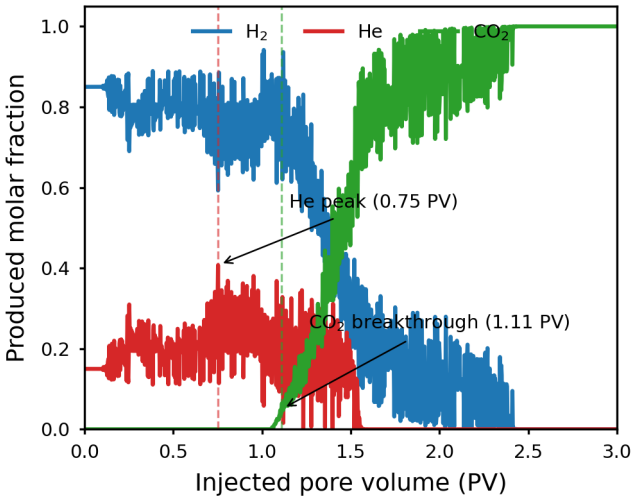


Fig. 3. Produced molar fraction versus injected pore volume in the heterogeneous reservoir. The helium peak and the CO_2 breakthrough delimit the staged recovery.

Table 2. Retardation-factor decomposition and mechanism classification.

Component	R_{ads}	R_{diss}	R_{tot}	Mechanism class
He	1.000	1.001	1.001	advection-dominant (Knudsen-enhanced)
H_2	1.284	1.003	1.287	adsorption–advection–diffusion
CO_2	1.769	1.107	1.958	strong-adsorption retarded

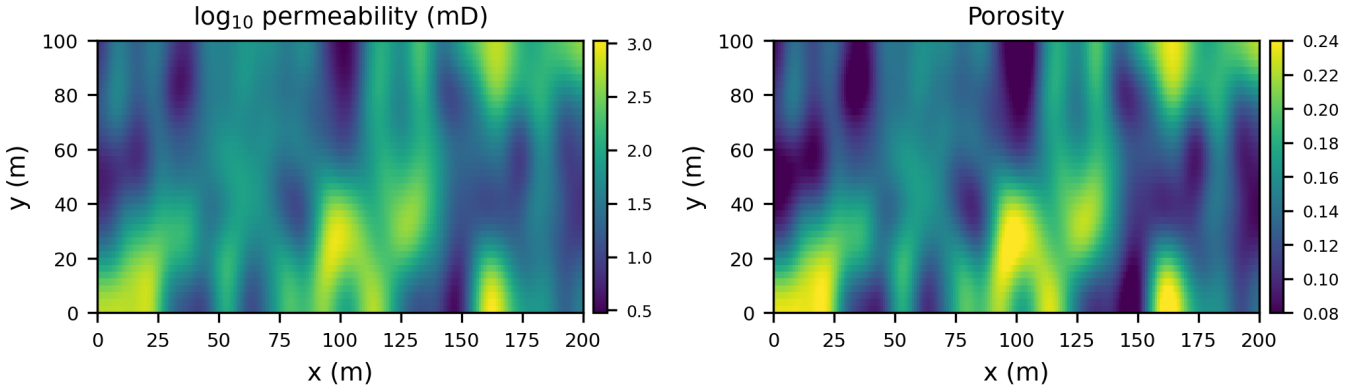


Fig. 1. Heterogeneous (a) $\log_{10}$ permeability and (b) porosity fields used in this study.

3.4 Selective displacement versus physical displacement

Fig. 4 and the integrated quantities provide the values used to evaluate the criterion defined in Eq. (7). Starting from an initial adsorbed H_2 inventory of 9.68×10^7 mol, CO_2 flooding reduces it to essentially zero ($\eta(H_2) = 1.00$), whereas the adsorbed He inventory remains at its negligibly small initial value ($\eta(He) = 0$). At the same time, the adsorbed CO_2 inventory grows from zero to 8.27×10^7 mol. The distinction between selective and physical displacement is therefore preserved in the heterogeneous reservoir: CO_2 flooding opens an adsorption-exchange recovery pathway for H_2 that does not exist for He, and injected CO_2 is itself retained by adsorption. The direction of this modeled behavior is consistent with experimental and molecular-scale evidence for preferential CO_2 adsorption, reduced H_2 surface occupancy in mixed-gas systems, and enhanced H_2 recovery in CO_2-containing breakthrough experiments (Alanazi et al., 2023, 2024; Muther and Dahaghi, 2024; Zhang et al., 2024; Zhang et al., 2024; Al-Harbi et al., 2025; Li et al., 2025).

3.5 Sensitivity of retention time to the adsorption Damköhler number

To validate the Da criterion in a clean setting, we swept the hydrogen adsorption capacity q_{max}, H_2 in a homogeneous reservoir while holding the He and CO_2 parameters fixed, and recorded the chromatographic retention time (the temporal centroid of the produced molar fraction) of H_2 and He (Fig. 5). Three observations follow. First, the H_2 retention time increases monotonically with $Da(H_2)$ in the low-Da regime, from 0.612 PV at Da = 0.067 to a plateau near 0.776 PV, whereas the He retention time stays at 0.576 PV regardless of $Da(H_2)$. The H_2–He retention-time difference therefore grows from 0.133 to about 0.200 PV. Second, the increase saturates for $Da(H_2) \geq 0.5$. This model-specific plateau arises from the bounded extended Langmuir relation (Kapoor et al., 1990) and CO_2-driven displacement; the underlying adsorption contrast is qualitatively consistent with published studies (Alanazi et al., 2023; Wang et al., 2023; Muther and Dahaghi, 2024; Zhang et al., 2024; Zhang et al., 2024; Al-Harbi et al., 2025). The nonlinear plateau departs from the linear chromatographic prediction (Chabab et al., 2024). Third, at very low Da (below 0.17), the retention-time difference becomes slightly negative within the present model, indicating that the model's Knudsen-enhanced helium diffusion dominates the vanishing adsorption contrast. This sign reversal shows why a dual Da-Pe criterion, rather than a single number, is needed; it also provides a point of comparison with recent dimensionless pore-scale H_2-CO_2 transport analysis (Purswani et al., 2024).

3.6 Effect of heterogeneity on hydrogen–helium separation

Within the present model, heterogeneity primarily modulates the magnitude of hydrogen–helium separation. The helium enrichment peak falls from 0.541 (homogeneous) to 0.407 (heterogeneous), and CO_2 breakthrough advances from 1.60 PV to 1.11 PV because preferential channels let CO_2 reach the producer early while low-permeability lenses disperse the helium slug. The two modeled mechanistic signatures nevertheless survive: helium is still swept ahead of hydrogen, and the displacement-efficiency pair remains $\eta(H_2) \approx 1$ and $\eta(He) = 0$. Within the parameter range examined here, molecular adsorption properties retain the ordering of the transport regimes, whereas permeability heterogeneity mainly alters local velocities, sweep patterns, and breakthrough timing in

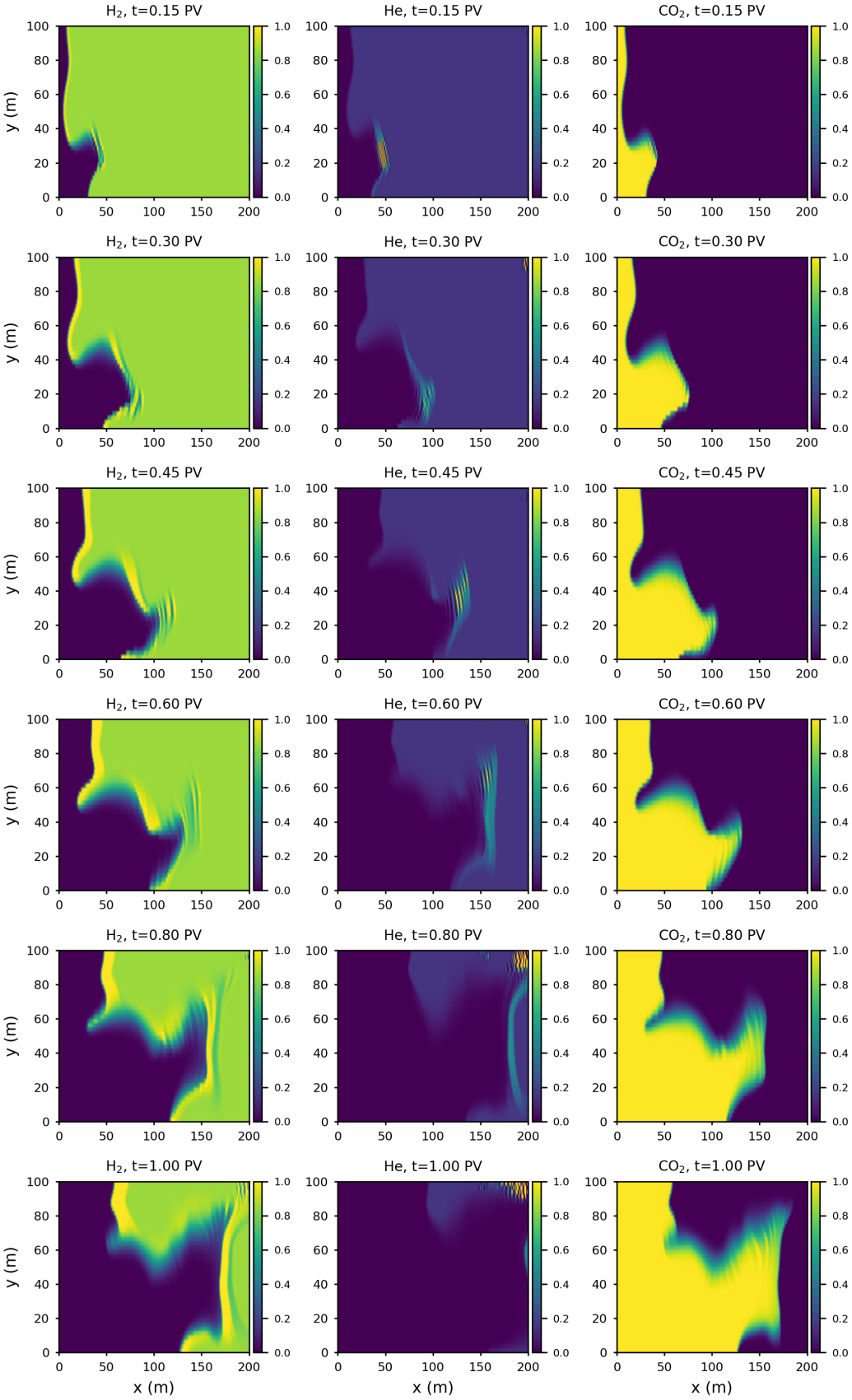


Fig. 2. Molar-fraction maps of H_2, He, and CO_2 in the heterogeneous reservoir at six injected pore volumes, showing the distorted front, preferential channels, and the helium-enriched slug.

the present simulations. Prior underground hydrogen-storage studies likewise show that reservoir architecture and permeability–porosity distributions affect gas mixing and recovery (Bo et al., 2024; Khandoozi et al., 2025; Lu et al., 2025). Separate simulations under homogeneous rock properties show that lateral gas separation can reduce mixing when CO_2 is used as a cushion gas (Williams et al., 2025). Early CO_2 breakthrough narrows the window for capturing the helium-rich stream, making well placement and sweep management important design variables in the present heterogeneous model. By contrast, the selective-displacement pathway for hydrogen remains active in the present simulations, consistent with experimental evidence that CO_2-containing mixtures can improve H_2 recovery (Li et al., 2025).

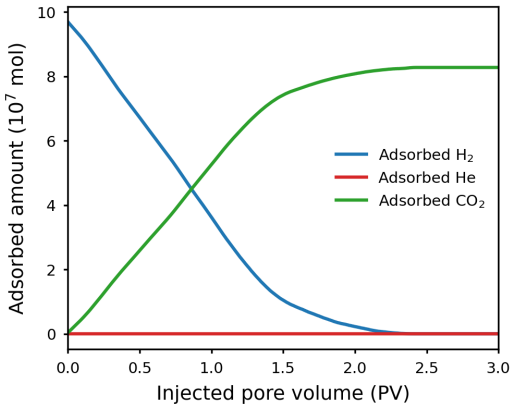


Fig. 4. Evolution of adsorbed amounts during CO_2 flooding in the heterogeneous reservoir. Adsorbed H_2 is nearly fully displaced, adsorbed He is unaffected, and CO_2 is itself adsorbed.

Taken together, the results suggest a decoupled design strategy for co-production: Enhance hydrogen recovery through CO_2 competitive adsorption, which is robust to heterogeneity, and protect helium recovery through sweep management and early-time capture, which is where heterogeneity matters most.

4. Concluding remarks

We have built a coupled theoretical–numerical framework that quantitatively discriminates the transport mechanisms of hydrogen and helium in natural hydrogen–helium reservoirs under CO_2 flooding, including the effect of geological heterogeneity. The principal conclusions are as follows.

1) Hydrogen and helium belong to distinct transport-mechanism classes. In a dimensionless Damköhler–Péclet framework, helium is advection-dominant with Knudsen enhancement, hydrogen exhibits coupled adsorption, advection, and diffusion, and CO_2 is strongly retarded by adsorption, with retardation factors of 1.001, 1.287, and 1.958, respectively. The classification is validated by a monotonic and then saturating increase in the H_2-He retention-time difference with the Damköhler number.
2) CO_2 flooding discriminates the two gases through different mechanisms. The displacement-efficiency coefficient derived from competitive adsorption gives $\eta(H_2) \to 1$ (selective displacement of adsorbed hydrogen) and $\eta(He) \equiv 0$ (purely physical displacement), while the injected CO_2 is itself adsorption-trapped.
3) The mechanistic divergence enables staged, time-zoned co-production that persists under geological heterogeneity. Unretarded helium accumulates as an enriched slug ahead of the retarded hydrogen and the CO_2 front, reaching a mole-fraction peak of 0.407 (2.7-fold enrichment) even in a reservoir whose permeability spans more than two orders of magnitude. Heterogeneity advances CO_2 breakthrough and disperses the helium slug, but leaves the mechanisms, and therefore the selective-displacement and physical-displacement criteria, unchanged.

The present model adopts a single mobile gas phase, an ideal-gas equation of state, equilibrium aqueous partitioning, and an effective representation of Knudsen and slip transport. Recent pore-scale and reservoir-scale studies indicate that relative-permeability hysteresis, gas–brine interfacial effects, and geochemical reactions may become important under realistic storage conditions (Adam et al., 2024; Higgs et al., 2024; Davoodi et al., 2025). Incorporating these processes together with real-gas thermodynamics, component-dependent viscosity, and three-dimensional well configurations is therefore a natural extension of the present framework.

Acknowledgements

We would like to express our appreciation for the following financial support: National Key Research and Development Project of China (Grant No. 2023YFA1011701), Shandong Excellent Young Scientist (Overseas) Program (No.2024HWYQ–050), and the Postdoctoral Fellowship Program of CPSF under Grant Number GZC20250432.

Conflict of interest

The authors declare no competing interest.

Open Access This article is distributed under the terms and conditions of the Creative Commons Attribution (CC BY-NC-ND) license, which permits unrestricted use, distribution, and reproduction in any medium, provided the original work is properly cited.

References

Alanazi, A., Abid, H., Bawazeer, S. A., et al. Hydrogen and carbon dioxide kinetic adsorption and diffusion behavior into organic-rich shale: Implications of mineralogy and organic content. Energy & Fuels, 2024, 38(23): 23009-23024.

Alanazi, A., Abid, H. R., Usman, M., et al. Hydrogen, carbon dioxide, and methane adsorption potential on Jordanian organic-rich source rocks: Implications for underground H2 storage and retrieval. Fuel, 2023, 346: 128362.

Al-Harbi, A., Abdel-Azeim, S., Saad, M., et al. Adsorption and diffusion behavior of pure H_2, and H_2/CO_2, H_2/CH_4 mixtures in sandstone-rich clay shale reservoirs: Insights from molecular dynamics simulations. International Journal of Hydrogen Energy, 2025, 170: 151214.

Adam, A. M., Bahamon, D., Al Kobaisi, M., et al. Molecular dynamics simulations of the interfacial tension and

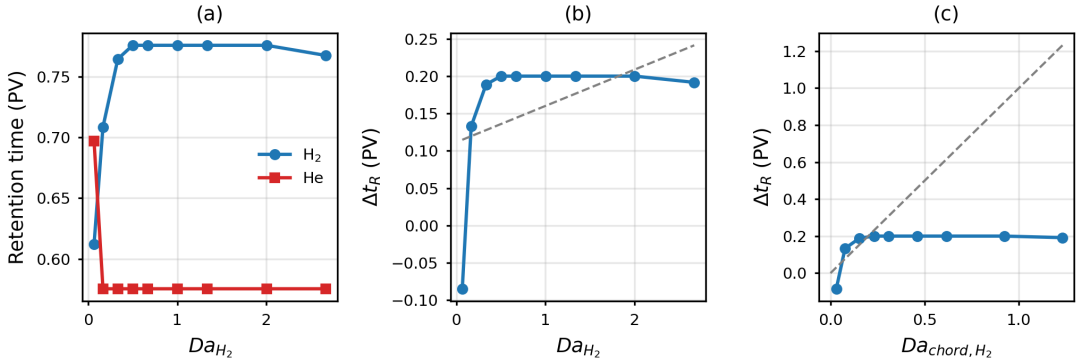


Fig. 5. Retention time versus adsorption Damköhler number (homogeneous setting). (a) H_2 retention time rises and saturates while He stays constant; (b) the H_2–He retention-time difference grows monotonically before saturating; (c) the deviation from the linear chromatographic relationship reflects Langmuir saturation.

the solubility of brine/H_2/CO_2 systems: Implications for underground hydrogen storage. International Journal of Hydrogen Energy, 2024, 78: 1344-1354.

Ballentine, C. J., Karolytė, R., Cheng, A., et al. Natural hydrogen resource accumulation in the continental crust. Nature Reviews Earth & Environment, 2025, 6: 342-356.

Bo, Z., Hörning, S., Underschultz, J. R., et al. Effects of geological heterogeneity on gas mixing during underground hydrogen storage (UHS) in braided-fluvial reservoirs. Fuel, 2024, 357: 129949.

Chabab, S., Kerkache, H., Bouchkira, I.,et al. Solubility of H_2 in water and NaCl brine under subsurface storage conditions: Measurements and thermodynamic modeling. International Journal of Hydrogen Energy, 2024, 50: 648-658.

Davoodi, S., Al-Shargabi, M., Wood, D. A., et al. Underground hydrogen storage: A review of technological developments, challenges, and opportunities. Applied Energy, 2025, 381: 125172.

Higgs, S., Da Wang, Y., Sun, C., et al. Direct measurement of hydrogen relative permeability hysteresis for underground hydrogen storage. International Journal of Hydrogen Energy, 2024, 50: 524-541.

Kapoor, A., Ritter, J. A., Yang, R. T. An extended Langmuir model for adsorption of gas mixtures on heterogeneous surfaces. Langmuir, 1990, 6(3): 660-664.

Khandoozi, S., Li, P., Ershadnia, R., et al. An integrated approach for optimizing geological hydrogen storage. Applied Energy, 2025, 381: 125182.

Li, P., Liu, Q., Zhu, D., et al. Distributions and accumulation mechanisms of helium in petroliferous basins. Science China Earth Sciences, 2024, 67(10): 3143-3168.

Li, Y., Wang, K., Sun, Q. Experimental investigations on the dynamic transport characteristics of H_2, CO_2, and CH_4 gas mixtures in shale: Implications for underground hydrogen storage. International Journal of Hydrogen Energy, 2025, 138: 582-594.

Lu, J., Muhammed, N. S., Okolie, J. A., et al. A sensitivity study of hydrogen mixing with cushion gases for effective storage in porous media. Sustainable Energy & Fuels, 2025, 9(5): 1353-1370.

Mao, S., Yu, S., Xu, J., et al. Geologic hydrogen: A review of resource potential, subsurface dynamics, exploration, production, transportation, and research opportunities. Energy & Environmental Science, 2025, 18(23): 9991-10035.

Muther, T., Dahaghi, A. K. Monte-Carlo simulations on H_2 adsorption in kaolinite nanopore in the presence of CO_2 and CH_4 gases. Fuel, 2024, 365: 131249.

Potter, R. W., Clynne, M. A. The solubility of the noble gases He, Ne, Ar, Kr, and Xe in water up to the critical point. Journal of Solution Chemistry, 1978, 7(11): 837-844.

Purswani, P., Guiltinan, E. J., Chen, Y., et al. Pore-scale modeling of carbon dioxide and hydrogen transport during geologic gas storage. Geophysical research letters, 2024, 51(12): e2024GL109216.

Roe, P. L. Characteristic-based schemes for the Euler equations. Annual review of fluid mechanics, 1986, 18(1): 337-365.

Richardson, J. F. Particle technology and separation processes in Coulson and Richardson's chemical engineering, edited by J. F. Richardson., J. H. Harker and J. R. Backhurst, Butterworth-Heinemann, Oxford, pp. 1078, 2002.

Sander, R. Compilation of Henry's law constants (version 5.0. 0) for water as solvent. Atmospheric Chemistry and Physics, 2023, 23(19): 10901-12440.

Scholes, C. A., Ghosh, U. K. Review of membranes for helium separation and purification. Membranes, 2017, 7(1): 9.

Van Leer, B. Towards the ultimate conservative difference scheme. V. A second-order sequel to Godunov's method. Journal of computational Physics, 1979, 32(1): 101-136.

Wei, Y., Liu, Q., Zhu, D., et al. Helium and natural hydrogen in the Bohai Bay Basin, China: Occurrence, resources, and exploration prospects. Applied Energy, 2025, 383: 125398.

Wang, L., Cheng, J., Jin, Z., et al. High-pressure hydrogen adsorption in clay minerals: Insights on natural hydrogen exploration. Fuel, 2023, 344: 127919.

Wolff-Boenisch, D., Abid, H. R., Tucek, J. E., et al. Impor-

tance of clay-H_2 interactions for large-scale underground hydrogen storage. International Journal of Hydrogen Energy, 2023, 48(37): 13934-13942.

Williams, H. A., Heinemann, N., Molnar, I. L., et al. Hydrogen storage in depleted gas reservoirs with carbon dioxide as a cushion gas: Exploring a lateral gas separation strategy to reduce gas mixing. International journal of hydrogen energy, 2025, 102: 1116-1129.

Zgonnik, V. The occurrence and geoscience of natural hydrogen: A comprehensive review. Earth-Science Reviews, 2020, 203: 103140.

Zhang, Q., Masoudi, M., Sun, L., et al. Hydrogen and cushion gas adsorption–desorption dynamics on clay minerals. ACS Applied Materials & Interfaces, 2024, 16(40): 53994-54006.

Zhang, M., Yang, Y., Pan, B., et al. Molecular simulation on H_2 adsorption in nanopores and effects of cushion gas: Implications for underground hydrogen storage in shale reservoirs. Fuel, 2024, 361: 130621.